Journal of Sound and Vibration 333 (2014) 1767–1780

Contents lists available at ScienceDirect

Journal of Sound and Vibration

journal homepage: www.elsevier.com/locate/jsvi

Revisiting a magneto-elastic strange attractor

Jee Ian Tam [a], Philip Holmes [a,b,*]

[a] Department of Mechanical and Aerospace Engineering, Princeton University, Princeton, NJ 08544, USA
[b] Program in Applied and Computational Mathematics, Princeton University, Princeton, NJ 08544, USA

ARTICLE INFO

Article history:
Received 4 August 2013
Received in revised form
29 October 2013
Accepted 11 November 2013
Handling Editor: Ivana Kovacic
Available online 9 December 2013

ABSTRACT

We revisit an early example of a nonlinear oscillator that exhibits chaotic motions when subjected to periodic excitation: the magneto-elastically buckled beam. In the paper of Moons and Holmes (1980) [1] magnetic field calculations were outlined but not carried through; instead the nonlinear forces responsible for creation of a two-well potential and buckling were fitted to a polynomial function after reduction to a single mode model. In the present paper we compute the full magnetic field and use it to approximate the forces acting on the beam, also using a single mode reduction. This provides a complete model that accurately predicts equilibria, bifurcations, and free oscillation frequencies of an experimental device. We also compare some periodic, transient and chaotic motions with those obtained by numerical simulations of the single mode model, further illustrating the rich dynamical behavior of this simple electromechanical system.

1. Introduction

In this paper we return to a classical problem in nonlinear vibrations: the single degree-of-freedom (dof) Düffing's equation [2] with an unstable equilibrium flanked by two stable equilibria. Unlike the stiffening spring case considered in many textbooks, e.g. [3], the two-well potential energy of this system endows its phase space with a homoclinic orbit [4] which undergoes global bifurcations that produce non-periodic, chaotic motions when external periodic forcing is applied. This mathematical model with its physical analog of an elastic cantilever beam buckled by ferromagnetic forces, exemplified in Fig. 1, has become a central example in "chaos theory" since its introduction in 1979 [1], e.g. see [5,6].

The simplest model for a single dof oscillator with a two-well potential has a symmetric cubic restoring force and linear damping. With additive sinusoidal forcing, the ODE takes the form

$$\ddot{x}+\delta\dot{x}-\alpha x+\beta x^3=P\ \cos(\omega t), \tag{1}$$

where the parameters $\alpha,\ \beta,\ \omega>0$, and $\delta,\ P\geq 0$. When $P=\delta=0$, Eq. (1) is a Hamiltonian system that conserves energy

$$H(x,\dot{x})=\frac{\dot{x}^2}{2}-\frac{\alpha x^2}{2}+\frac{\beta x^4}{4}, \tag{2}$$

so that orbits of Eq. (1) lie on level sets of $H(x,\dot{x})$ [4] and we observe a double homoclinic loop containing a saddle point on the set $H(x,\dot{x})=0$. Perturbing from this integrable case, it was proved in [7] that, for fixed $\alpha,\ \beta,\ \omega>0$, $0<\varepsilon\ll 1$, $\delta,P=\mathcal{O}(\varepsilon)$ and $P>\delta P_c(\alpha,\beta,\omega)$ (a critical value, see Eq. (14) below), Eq. (1) has transverse homoclinic orbits and therefore possesses a chaotic invariant set containing infinitely many unstable periodic orbits: a Smale horseshoe [4, Sections 4.5 and 5.1]. An analogous result was subsequently proved for a PDE modeling vibrations of a simply supported buckled beam [8] and there have been numerous similar studies of systems with 2 or more degrees of freedom, e.g. [9–11].

* Corresponding author.
E-mail address: pholmes@math.princeton.edu (P. Holmes).

0022-460X/$ - see front matter © 2013 Elsevier Ltd. All rights reserved.
http://dx.doi.org/10.1016/j.jsv.2013.11.022

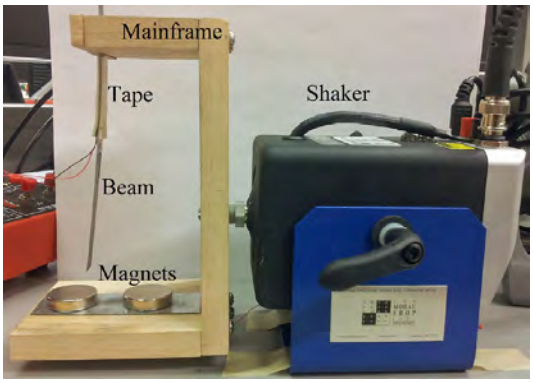

Fig. 1. The magneto-elastic beam and shaker. The frame measures $153 \times 100 \times 76\ \mathrm{mm}^3$.

These results do not imply that Eq. (1) has a strange attractor [4] (indeed, the stable manifolds of the horseshoe may form a fractal basin boundary separating the domains of attraction of two stable periodic orbits that "grow" from the stable equilibria of (1) for $P=0$ [6,4]), but many subsequent studies and analyses of Poincaré maps strongly suggest that there are open (or at least measurable) sets in parameter space for which strange attractors do exist. For an introductory article with animations, see [12].

The present paper revisits the analysis of [1], augmenting it with explicit numerical calculations of the magnetic field, from which the nonlinear stiffness term in the single dof model may be derived explicitly. We compare the resulting function with the cubic of Eq. (1), fitting the parameters α and β from experimental observations of equilibrium positions and natural frequencies and deriving the damping factor δ from free vibration decay rates. We find that the model calculations predict key quantities within 10 percent, and that bifurcation diagrams also match experimental results well, including transitions from two to three stable equilibria and symmetry-breaking as magnet positions vary with respect to the clamped end of the beam.

This paper is organized as follows. We first describe the magneto-elastic beam used for experimental data collection in Section 2, since this simple physical system also underlies the model. In Section 3 we review the partial differential equation (PDE) describing the beam and outline its reduction by Galerkin's method to an ordinary differential equation (ODE) describing the fundamental flexural mode. The analysis follows [1], supplemented by a recent efficient algorithm due to Derby and Olbert [13] that is used to compute the magnetic field and resulting restoring forces. Polynomial approximations to the restoring forces are also derived, analogous to those considered in [1]. In Section 4 we compare predictions of equilibrium positions and natural frequencies derived from the single mode model of Section 3 with experimental measurements, and illustrate bifurcations of equilibria that occur under changes in the magnetic field due to magnet placement relative to the beam's support. The dynamics of periodically forced vibrations are considered in Section 5, including subharmonics and non-periodic, chaotic motions, which are studied using Poincaré maps. Conclusions and a brief discussion follow in Section 6.

2. The experimental rig

The physical system, shown in Fig. 1, is a slender steel cantilever beam clamped in a nominally rigid frame at its upper end and free at its lower end. The beam moves under the influence of elastic, magnetic, and noninertial forces (when the frame is excited horizontally by the shaker). Gravitational forces also act, but these are much smaller than the forces noted above and will be neglected in the model developed in Section 3.

The frame is fabricated in 12.3 mm thick maple hardwood with the grain oriented longitudinally in each component. Components are joined by 3 woodscrews at top and bottom and a strip of 1018 steel is glued to the upper surface of the base for magnet attachment. The beam is 1095 blue tempered spring steel of Young's modulus $E=2.06\times10^5$ MPa, density $\rho=(7.83\pm0.02)\times10^3\ \mathrm{kg\ m}^{-3}$, with thickness $\Delta=0.25\pm0.02$ mm and width $w=9.5\pm0.5$ mm, clamped at the top of the frame by a maple strip secured by 2 woodscrews. To increase damping, strips of Scotch tape 39.2 ± 0.1 mm long, 9.6 ± 0.1 mm wide and 1.5 ± 0.2 mm thick are attached to both sides of the beam near the clamp. Experiments were conducted with free beam length $L=96.1\pm0.5$ mm below the clamp and distance from beam tip to frame base 19.2 ± 0.5 mm. Beam dimensions were chosen so that the fundamental flexural mode is well separated in frequency from torsional and higher flexural modes.

Two cylindrical rare earth magnets of radius $r=12.7$ mm, height $h=0.635$ mm and surface field strength $B_{\mathrm{surface}}=0.21$ Tesla are placed with matching N–S polarities on the steel strip, whose upper surface is roughened to prevent magnet movement. Magnet center positions can be varied upward from a minimum separation of 37.4 ± 0.1 mm. Most of the experiments are done with magnet centers (approximately) equally spaced from the undeflected beam tip, but asymmetric cases are also considered. The frame is attached to the driving shaft of the shaker by a machine screw whose axis passes through the frame's mass center, as computed from the assembly with magnets as modeled in Creo Pro/Engineer. Sinusoidal excitation is provided by a K2007E01 SmartShaker electromagnetic shaker with an integrated amplifier (The Modal Shop,

Cincinnati, OH) driven by an Agilent 33220A signal generator (Agilent Technologies, Santa Clara, CA) that allows frequency and peak-to-peak voltage to be varied. The signal generator output is monitored on an oscilloscope. The shaker-frame assembly is assumed sufficiently rigid that shaker and frame motions are indistinguishable.

An SGD-7/350-LY11 Omega strain gauge (Omega, Stamford, CT) with 350 Ω resistance and 2.13 gauge factor is attached with Loctite 401 adhesive to the beam's surface near its root. Strain gauge output is fed to a custom built Wheatstone quarter-bridge circuit, temperature compensated by a second Omega strain gauge, and then to an AD623 Instrumentation Amplifier (Analog Devices, Norwood, MA). A potentiometer connected to a positive voltage at one side and the AD623's reference input at the other allows calibration of the amplifier output as proportional to beam tip displacement, and this output is passed through an op-amp differentiator circuit to provide beam tip velocity. Displacement and velocity signals pass to an Arduino Uno microcontroller with a 10-bit Analog-to-Digital converter and an 8-bit ATmega328 microcontroller (Adafruit Industries, NYC), and thence to a laptop for data analysis. A mean sampling rate of 620 ± 20 Hz was achieved, with uncertainty of ± 5 digital units in position and ± 10 digital units in velocity in the full $2^{10}=1024$ unit range.

Further details of the experimental apparatus and data collection circuits are provided in [14].

3. An elastic beam in a nonlinear magnetic field

In this section we review the PDE model of [1] for the magneto-elastic beam and the single dof reduction that describes the dynamics of its fundamental mode of vibration. We also describe how the field model for an ideal solenoid of [13] is used to compute magnetic forces induced in the beam.

3.1. The cantilever beam model: linear elasticity

Fig. 2 shows the coordinate system used to describe the state of a slender uniform clamped beam of length L, width w and thickness $\Delta \ll w$. Here s denotes arclength along the undeformed beam's centerline and $u(s,t), v(s,t)$ denote displacements in the x, y directions respectively. We have already noted that gravitational forces are neglected. Since flexural displacements and strains are relatively small (maximum tip displacements are ≈ 15 percent of beam length, cf. Fig. 1) and the beam is thin ($\Delta = 0.026w$), we assume linear elasticity and use inextensible Euler–Bernoulli beam theory [15, Chapter 7]. Hence the tangent angle $\theta \approx \partial v/\partial s$ and flexural vibrations are described by the following PDE for $v = v(s,t)$:

$$F_y(s,v) - EIv'''' - C'(s,v) + [T(s,v)v']' = m[\ddot{v} + \ddot{V}_0(t)], \tag{3a}$$

$$\text{where} \quad T(s,v) = \int_s^L F_x(s,v)\, \mathrm{d}s. \tag{3b}$$

Here $v' = \partial v/\partial s$, $\dot{v} = \partial v/\partial t$, $EI = E(w\Delta^3/12)$ is the flexural rigidity of the beam, m its mass per unit length, $V_0(t)$ the displacement imposed on the frame supporting it; F_x, F_y are the x,y components of magnetic forces per unit length, C is the moment per unit length due to magnetic forces and T is the axial tension due to F_x. Note that these magnetic terms depend upon the location of points along the beam (s,v), and that they are the sole source of nonlinearity in the model; all elastic and inertial forces are linear. Thus far we have neglected dissipative effects; they will be included after reduction to a single mode.

As in [1], the sinusoidal forcing $V_0(t)$ is chosen to excite the first mode of vibration, and displacements remain small. We therefore assume that the beam's shape is well approximated by the fundamental mode of an Euler–Bernoulli clamped-free cantilever described by $-EIv'''' = m\ddot{v}$ with boundary conditions $v(0,t) = v'(0,t) = 0$ and $v''(L,t) = v'''(L,t) = 0$. This eigenvalue problem is solved by

$$\phi(s) = c[K(\sinh(ks) - \sin(ks)) + (\cosh(ks) - \cos(ks))], \tag{4a}$$

where

$$\cosh(kL)\cos(kL) = -1 \quad \text{and } K = -\frac{\cos(kL) + \cosh(kL)}{\sin(kL) + \sinh(kL)}, \tag{4b}$$

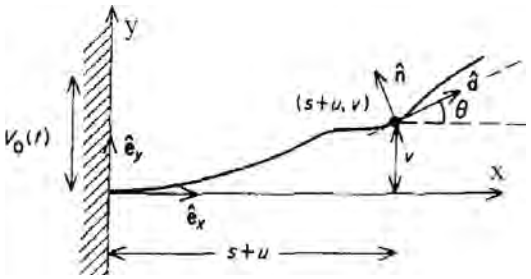

Fig. 2. Coordinate system for the cantilever beam; note that the coordinate frame $\hat{\mathbf{e}}_x, \hat{\mathbf{e}}_y$ is rotated in comparison to the physical system of Fig. 1. From [1, Fig. 4(a)].

implying that $kL \approx 1.875104$ and $K \approx -0.734096$ [16, Section 9.5]. The normalization constant c is chosen so that $\int_0^L \phi^2 \, ds = 1$. Setting $v(s,t) = a(t)\phi(s)$ and projecting Eq. (3) onto the subspace spanned by the mode $\phi(s)$ using the usual inner product, integrating by parts and using the boundary conditions to eliminate some terms, we obtain

$$m\ddot{a} = -\int_0^L [EI(\phi'')^2 a - F_y(s,a)\phi' + T(s,a)(\phi')^2 a - C(s,a)\phi' - m\ddot{V}_0\phi] \, ds. \tag{5}$$

For future use, we separate the elastic and magnetic restoring force terms and add a linear damping term. Also, since it is convenient to describe the beam's state in terms of its tip displacement, we use the fact that $v(L,t) = a(t)\phi(L) \stackrel{\text{def}}{=} v_L(t)$ to rewrite Eq. (5) as

$$\ddot{v}_L = F_{\text{beam}}(v_L) + F_{\text{magnetic}}(v_L) - \delta\dot{v}_L - \ddot{V}_0 \int_0^L \phi \, ds, \tag{6}$$

where $F_{\text{beam}}(a) = -EI \int_0^L (\phi'')^2 a \, ds/m$ and $F_{\text{magnetic}}(a)$ is defined analogously from Eq. (5). The magnetic field terms F_y, $T = \int_0^L F_x(s,v) \, ds$ and C depend on the beam's location, which is specified by $\phi(s)$ and $a(t)$, or, equivalently $v_L(t)$. We now describe how these terms are computed.

3.2. The magnetic field: nonlinear restoring forces

We assume that the cylindrical magnets act as ideal solenoids and use the algorithm proposed in [13] to compute the magnetic field due to a solenoid using a generalized complete elliptic integral. This formulation contains the term nI, where n is the number of turns per unit length of the solenoid and I the current through it. We estimate nI from the field strength B_{surface} at the magnet's surface on its axis, as provided by the supplier, i.e., for a magnet of radius r and height h

$$nI = \frac{2B_{\text{surface}}}{\mu_0} \frac{\sqrt{h^2 + r^2}}{h}. \tag{7}$$

Eq. (7) is used with the explicit formulae and code for evaluating the integral given in [13]. See [14, Appendix F] for matlab codes that evaluate the force field in cylindrical coordinates.

We assume that the beam, whose width $w < r$, experiences the field $\mathbf{B} = (B_x(s,v), B_y(s,v))^T$ in the (x,y)-plane passing through the axes of both magnets uniformly across w. The magnetic forces $\mathbf{F} = (F_x(s,v), F_y(s,v))^T$ and the moment $\mathbf{C}(s,v)$ per unit length are [17,18]

$$\mathbf{F} = \mathbf{M} \cdot \nabla\mathbf{B}, \quad \mathbf{C} = \mathbf{M} \times \mathbf{B}, \tag{8}$$

where $\mathbf{M}$ is the magnetization per unit length of the beam. Neglecting magnetic hysteresis and self-forces on the beam and assuming that magnetization depends weakly on the beam's curvature, as in [1], we have

$$\mathbf{M} = \begin{pmatrix} M_x \\ M_y \end{pmatrix} = \frac{\chi A}{\mu_0 \mu_r} \begin{pmatrix} (1 + \chi \cos^2(\theta))B_x + \chi \cos(\theta) \sin(\theta) B_y \\ \chi \cos(\theta) \sin(\theta) B_x + (1 + \chi \sin^2(\theta))B_y \end{pmatrix}, \tag{9a}$$

$$C = |\mathbf{C}| = \frac{\chi^2 A}{2\mu_0 \mu_r} [2B_x B_y \cos(2\theta) - (B_x^2 - B_y^2) \sin(2\theta)]. \tag{9b}$$

Here θ is the tangent angle of the beam relative to the x-axis (Fig. 2), $A = w\Delta$ is the cross-sectional area, $\chi \approx 10^3$ [19] is the volumetric magnetic susceptibility of the beam material, $\mu_r = \chi + 1$ is the relative magnetic permeability and $\mu_0 = 4\pi * 10^{-7}$ N/A^2 is the magnetic constant.

In the reduced model $\theta(s, v_L) = v_L(t)\phi'(s)$. We calculate spatial derivatives of $\mathbf{B}$, $\mathbf{M}$ using 4th order central finite differences [20] and a Cartesian grid with spatial length scale 10^{-8} mm. To discretize $s \in [0, L]$ the beam is partitioned into 1000 equispaced points s_j, and $F_{\text{magnetic}}(s, v_L)$ and F_{beam} are computed by the following pseudocode:

For each beam tip displacement v_L
  For each node s_j
    Calculate node displacement $v(s_j) = \frac{\phi(s_j)}{\phi(L)} v_L$ and angle $\theta = \frac{\phi'(s_j)}{\phi(L)} v_L$.
    For displaced node at $(s_j, v(s_j))$ calculate the magnetic field (B_x, B_y) and hence F_x, F_y and C as above.
    Evaluate $\phi(s_j)$, $(\phi'(s_j))^2$ and $(\phi''(s_j))^2$.
  End
  Evaluate the integrals in $F_{\text{magnetic}}(s, v_L)$ and $F_{\text{beam}}(s, v_L)$, Eqs. (5) and (6), using a trapezoidal rule.
  Sum $F_{\text{magnetic}}(v_L) + F_{\text{beam}}(v_L)$.
End

This procedure yields magnetic forces acting on the entire beam and incorporates their spatial variations in evaluating the integral terms in Eq. (5), unlike the heuristic model of [1], which assumed that only the beam's tip is magnetized and neglected the couple C, leading to an approximation in which the axial tension $T(s,v)$ is constant and the lateral force $F_y(L,v)$ on the tip is modeled by a cubic or quintic polynomial. Fig. 3 shows an example of the computed magnetic field.

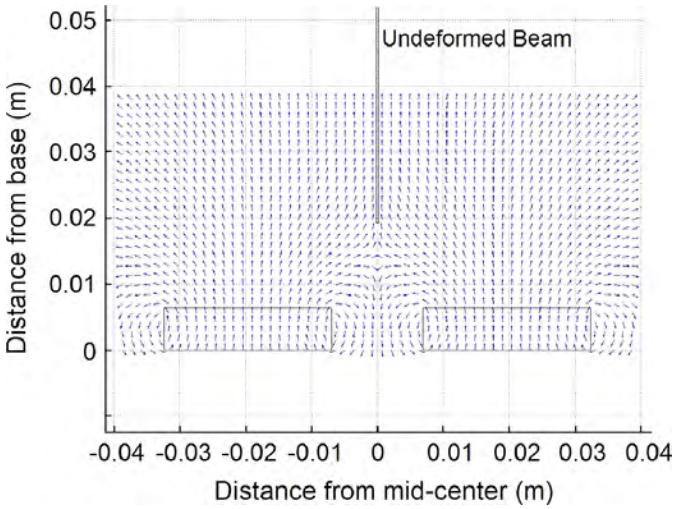

Fig. 3. Magnetic field in (x, y)-plane for magnet separation $d=4$ mm with vectors normalized in magnitude. Undeformed beam is shown with support on centerline between the magnets: zero offset case.

3.3. *The full model and cubic approximations*

Given the computations of Section 3.2, initial conditions and parameter values, Eq. (6) defines the system's dynamics. It will be solved in three forms:

1. *The full model*: compute $F_{\text{magnetic}}(v_L)+F_{\text{beam}}(v_L)$ from the magnetic field as in Section 3.2.
2. *The computational cubic approximation*: approximate $F_{\text{magnetic}}(v_L)+F_{\text{beam}}(v_L)$ by a cubic function as in Düffing's equation (1) with α and β chosen to yield the best fit over an appropriate range of tip displacements.
3. *The experimental cubic approximation*: determine α and β from the natural frequency of free vibrations and location of buckled equilibria in the physical system.

In all cases the damping factor δ is determined experimentally from decay rates of free vibrations.

These forms all have advantages and disadvantages. The full model is most accurate, given the reduction to a single mode and other approximations described above, but the restoring forces $F_{\text{magnetic}}(v_L)$ are only defined numerically ($F_{\text{beam}}(v_L)$ can be evaluated explicitly). The computational cubic approximation is less accurate, but offers a good approximation for small deflections, as will be explored below. Moreover, the dynamics of Düffing's equation have been analyzed extensively [7,4] and exact and perturbative solutions are known. The coefficients α, β, permit easy comparison of magnitudes of linear forces (both elastic and magnetic), nonlinear magnetic forces, and comparison of experimental data to model predictions.

4. Results 1: Free vibrations and bifurcations

We first consider the unforced system, starting without magnets to check the accuracy of the Euler–Bernoulli model for elastic forces by comparing natural frequency predictions with data, and to estimate the damping factor. We then add magnets, compare the predicted and experimental equilibrium positions, compute the coefficients α and β of the Düffing equation approximations, and investigate bifurcations as magnet positions are varied.

4.1. *Natural frequency and damping without magnets*

In the absence of magnetic forces and with $\ddot{v}_0=0$, Eq. (6) reduces to

$$\ddot{v}_L = -\left[\frac{EI\int_0^L(\phi''(s))^2\,ds}{m}\right]v_L-\delta\dot{v}_L \tag{10}$$

with undamped natural frequency $\omega_0=\sqrt{EI\int_0^L(\phi'')^2\,ds/m}$, damping ratio $\zeta=\delta/2\omega_0$, and damped natural frequency $\omega_d=\omega_0\sqrt{1-\zeta^2}$ for $\zeta<1$ [21]. Henceforth frequencies will be given in Hertz, thus $f_0=\omega_0/2\pi$ Hz, etc. For the beam used in our experiment, we predict $f_0=17.81$ Hz.

With magnets removed and no external excitation, the beam was displaced and released and the tip displacement recorded. Fitting an exponential to the envelope of the time series provides an estimate of $\zeta\omega_0=3.10\pm0.05$ (Fig. 4), and Fast Fourier Transform (FFT) estimates $f_d=17.6\pm0.5$ Hz (not shown), resulting in $\zeta=0.028\pm0.0008$ and $f_0=17.6\pm0.5$ Hz, so the prediction $f_0=17.81$ lies within the error bounds. The corresponding value of $\delta=6.20\pm0.1$. Fig. 4 also shows a solution of Eq. (10) that is almost indistinguishable from the experimental data.

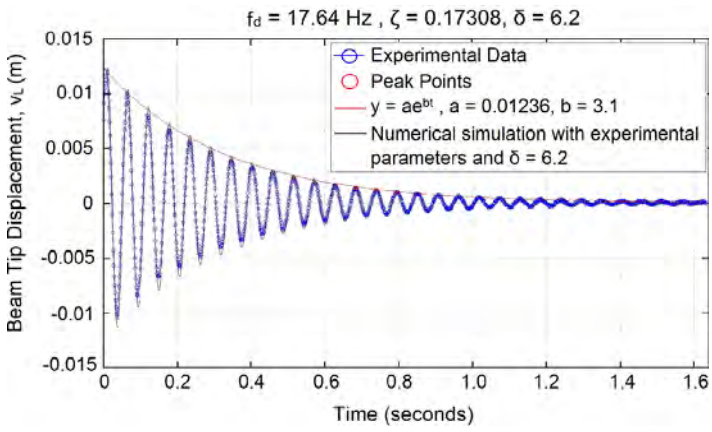

Fig. 4. Experimental time series, showing exponential fit and numerical simulation for damped oscillator Eq. (10).

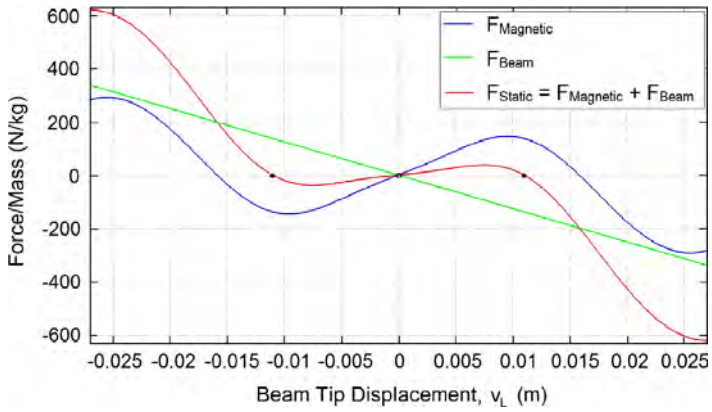

Fig. 5. Full model: contributions of F_{magnetic} (blue) and F_{beam} (green) to F_{static} (red) for $d=39.3$ mm. Stable and unstable equilibria indicated as dots and open circle. (For interpretation of the references to color in this figure caption, the reader is referred to the web version of this paper.)

4.2. Free vibrations with magnets

We now use experimental data obtained with the magnets in place to estimate coefficients in Düffing's equation with cubic restoring force. For $\delta>0$ the equilibria of Eq. (1) lie at $x=0$ and $x=\pm\sqrt{\alpha/\beta}$ and are respectively a saddle and a pair of sinks. Linearizing at the sinks reveals the damped natural frequency $f_{\pm}=\sqrt{2\alpha}/2\pi$. From this and the positions of these equilibria we can compute α and β. With magnet separation $d=39.3\pm0.2$ mm and offset (magnet asymmetry) nominally zero, the equilibria lie at -10 ± 0.02 mm and $+9.8\pm0.02$ mm, with natural frequencies 24.4 ± 0.1 Hz and 24.1 ± 0.1 Hz. Averaging these values to match the symmetry of the cubic, we find $\alpha=1.161\times10^4$ and $\beta=1.172\times10^8$. This is the experimental cubic approximation of Section 3.3. In both this case and computational approximation below, we use the damping factor $\delta=6.2$ obtained in Section 4.1.

We next estimate α and β from the full model, which predicts the restoring forces shown in Fig. 5, with zeroes of $F_{\text{static}}(v_L)=F_{\text{magnetic}}(v_L)+F_{\text{beam}}(v_L)$ at $v_L=0$ and $v_L=\pm0.011$ m. Seeking the cubic approximation that minimizes mean square error on the interval $v_L\in[-(d+r)/2,(d+r)/2]$ ($[-26,26]$ mm for $d=39.3$ and $r=12.7$), we find $\alpha=8.848\times10^3$ and $\beta=8.113\times10^7$ with equilibria at ±10 mm with natural frequency $f_{\pm}=21.2$ Hz. This is the computational cubic approximation of Section 3.3. Fig. 6 shows how the two cubic approximations of $F_{\text{static}}(v_L)$ compare to the full model. Although their α and β values differ by 27 percent and 31 percent respectively, their equilibrium positions both lie within 10 percent of the experimental ones. However, the full model provides a better approximation of the natural frequencies (24.45 ± 0.05 Hz, compared to the averaged experimental value 24.25 Hz), since the slopes of the full and experimental cubic curves agree better at the buckled equilibria.

Fig. 7(a) shows phase portraits in $(v_L,\dot{v}_L)$−space for the damped Düffing equation using the experimentally estimated parameters. The closed level sets of Eq. (2) are broken, and the interleaved domains of attraction of the two sinks are quite tightly wound for this lightly damped system. Three orbits obtained by releasing the beam tip at successively greater distances from $v_L=0$ are shown in Fig. 7(b), illustrating that they approach the right, left, and right sinks respectively as $v_L(0)$ increases. This figure shows that the tip displacement and velocity derived from the strain gauge are quite noisy, exhibiting non-physical self intersections for this planar, free-oscillation problem. Nonetheless, the experiment confirms the qualitative dependence on initial data predicted by the model.

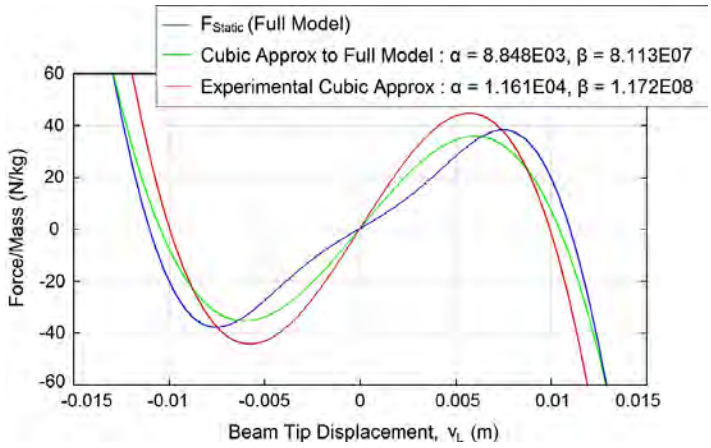

Fig. 6. Comparison of full model (blue), computational cubic approximation ($\alpha = 8.848 \times 10^3$, $\beta = 8.113 \times 10^7$, green) and experimental cubic approximation ($\alpha = 1.161 \times 10^4$, $\beta = 1.172 \times 10^8$, red) for F_{static}. (For interpretation of the references to color in this figure caption, the reader is referred to the web version of this paper.)

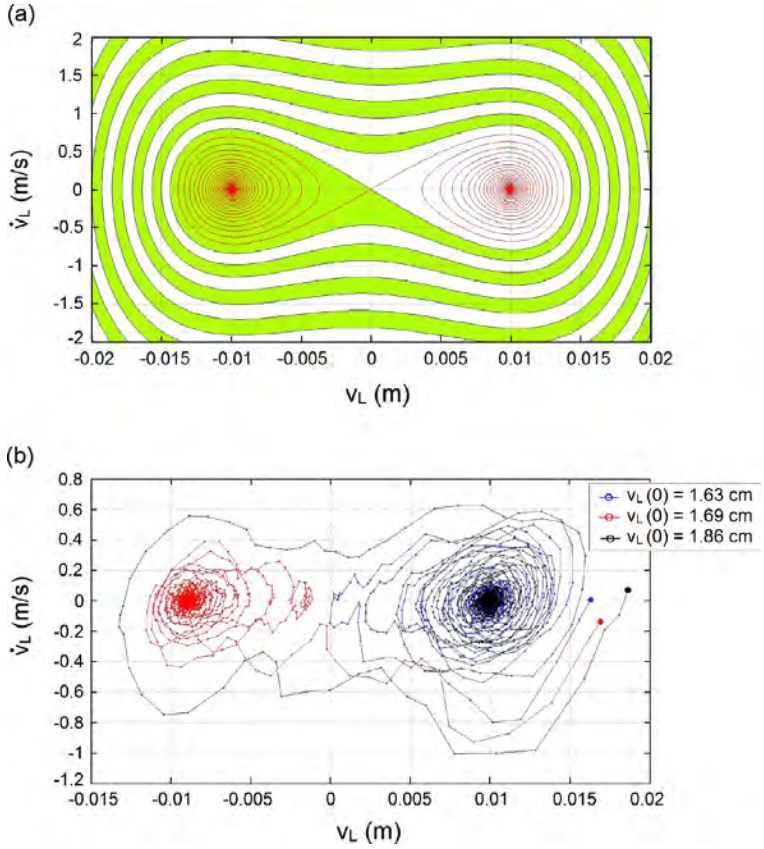

Fig. 7. (a) Basins of attraction for stable equilibria (white, green respectively) and stable and unstable manifolds of saddle point (blue, red) for Düffing's equation with experimental cubic parameters and damping $\delta = 6.2$. (b) Beam tip displacements for orbits approaching stable equilibria in the experiment; initial points are indicated as filled circles. (For interpretation of the references to color in this figure caption, the reader is referred to the web version of this paper.)

4.3. *Bifurcations of equilibria*

The magnetic field structure depends on the magnet positions (cf. Fig. 3) and the force field experienced by the beam depends on the location of the beam's support relative to the magnets. The latter can be parameterized by magnet spacing d and horizontal offset l of the point midway between the magnets relative to the beam's support. Variation of d and l reveal fairly complex behavior, including up to five equilibria, with three stable sinks. Other parameters such as magnet field strength and beam dimensions also affect forces, but they do not produce qualitatively different behavior [14], and our simple apparatus does not permit easy studies of their effects.

Fig. 8 shows the bifurcation diagram as magnet spacing d increases with zero offset, obtained by computing fixed points and their stabilities for the full model. All other physical parameters remain as above. The diagram is similar to that presented in [1, Fig. 6], including super- and sub-critical pitchfork bifurcations and symmetric saddle nodes [4]. Note that the full model predicts the experimentally observed stable equilibria within standard error bars, showing that its accuracy extends to larger magnet spacings, although the magnet and frame sizes do not allow exploration of the entire d range shown here.

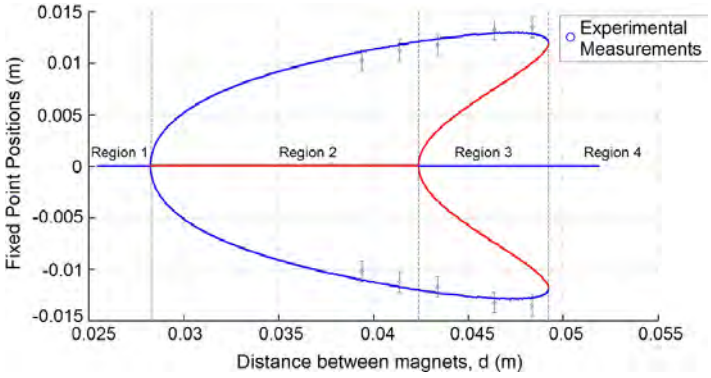

Fig. 8. Bifurcation diagram as distance between magnets d is increased. Solid curves are computed from the full model, circles are experimental data points with standard error bars; stable and unstable equilibria are shown in blue and red respectively. Stable equilibria were also observed near $v_L=0$ for $d>4.5$ mm, but reliable measurements were not obtained due to the weak magnetic field in the central region. (For interpretation of the references to color in this figure caption, the reader is referred to the web version of this paper.)

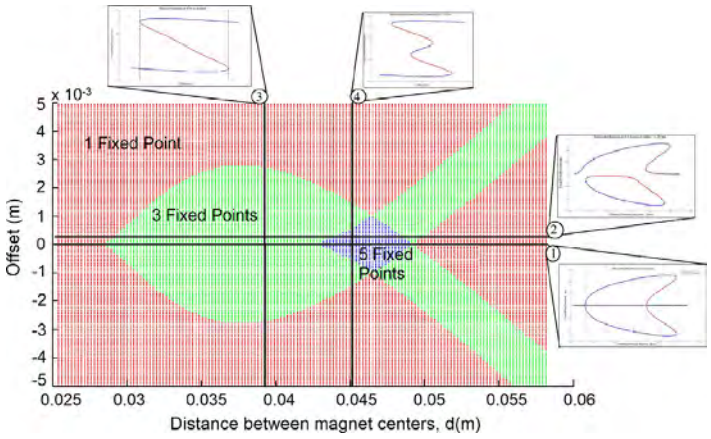

Fig. 9. Bifurcation set of the full model in (d,offset)-space, shown with 'slices' corresponding to bifurcation diagrams obtained by varying d (horizontal lines 1,2) and varying offset (vertical lines 3,4). Fig. 8 appears along line 1; a perturbed version with broken symmetry appears along line 2. Regions for which 1, 2 and 3 sinks exist are indicated. Saddle-node bifurcations occur on boundaries between these regions except along offset $=0$ line, on which pitchforks occur, except at rightmost point where 2 saddle nodes coincide.

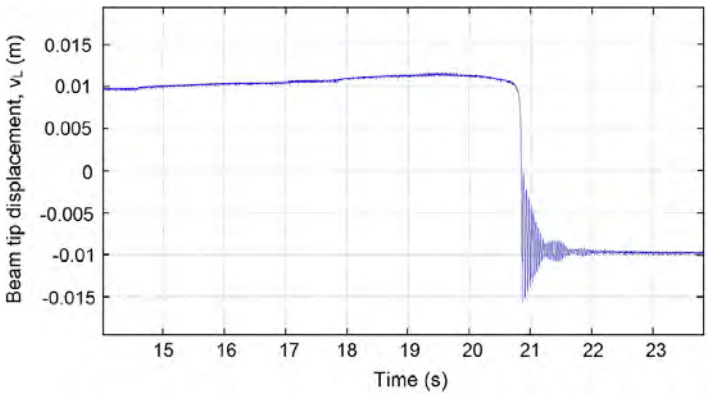

Fig. 10. Time series as one magnet moves away from the other with d increasing from 39.3 mm to 47.4 mm, passing a saddle-node bifurcation, after which the orbit rapidly transits to describe damped oscillations about a different stable fixed point.

Nonzero offsets break the reflection symmetry around $v_L=0$, causing the pitchfork bifurcations of Fig. 8 to locally break into a monotonic branch and a second branch that turns back in a saddle-node bifurcation [4, Section 7.1]. We illustrate this in the small inset associated with path 2 in the bifurcation set of Fig. 9. Other insets show that sequences of saddle nodes occur as offset varies for fixed d. Cubic approximations obviously fail to capture the saddle node bifurcations on the buckled branches and restabilization of the undeformed state that occurs for larger magnet spacings. A quintic polynomial restoring force can qualitatively reproduce this, as described in [1, Section 2.2, Figs. 5 and 6]. In fact the saddle-nodes and restabilizing pitchfork can collapse into a codimension 3 bifurcation point [4, Section 3.1] associated with the butterfly catastrophe [22], which involves unfolding a sixth-order polynomial potential function. This could be achieved experimentally by additionally varying the beam length L, and hence the vertical distance of its tip from the magnets.

To illustrate the dynamical consequences of a bifurcation, Fig. 10 shows the strain gauge signal as the inter-magnet distance d is increased by moving the right-hand magnet (1) away from the (fixed) left-hand magnet (2), starting with $d=39.3$ mm and offset $l=0$. This moves the system parameters (d, l) up and to the right, out of the region with 3 fixed points in Fig. 9. The stable fixed point at which the system state starts at $\approx +10$ mm is annihilated in a saddle-node bifurcation, after which the state jumps to the remaining stable fixed point at ≈ -10 mm.

5. Results 2: Forced vibrations

We now describe experiments in which the frame supporting the beam and magnets is subjected to sinusoidal displacement of frequency $f=\omega/2\pi$ and amplitude A_0, so that the external acceleration term in Eq. (6) is

$$V_0(t)=P\ \cos(\omega t), \quad \text{where } P=\omega^2 A_0\phi(L)\int_0^L \phi\ \mathrm{d}s. \tag{11}$$

Addition of periodic forcing to the single dof system increases its phase space dimension to three, since the vector field now depends on time. The third dimension is best interpreted as the phase of the applied oscillation, so that the phase space becomes $\mathbb{R}^2\times S^1$ and setting $v_l=v_1$ the ODE may be rewritten as

$$\begin{aligned}\dot{v}_1&=v_2,\\ \dot{v}_2&=F_{\text{static}}(v_1)-\delta v_2+P\ \cos(\omega\phi),\\ \dot{\phi}&=1.\end{aligned} \tag{12}$$

We then define a cross section $\Sigma_0=\{(v_1,v_2,\phi)|\phi=\phi_0\}$ at a fixed phase ϕ_0, and define the Poincaré map $\mathbf{P}:\Sigma_0\to\Sigma_0$ as

$$(v_1(n+1),v_2(n+1))=\mathbf{P}(v_1(n),v_2(n)), \tag{13}$$

[4] , where the point $(v_1(n+1),v_2(n+1))\in\Sigma_0$ is obtained by solving Eq. (12) for time $T=1/f$ with initial conditions $(v_1(n),v_2(n))$. This was done numerically for the full model and both cubic models using Matlab's ODE113 with relative and absolute tolerances of 10^{-10} and 10^{-8} respectively.

Equipment limitations prevented direct synchronization of the analog-to-digital converter with forcing phase ϕ_0. Experimental Poincaré maps were therefore obtained by linear interpolation of digitized data samples at intervals of $T=1/f$, taking f to be the frequency of the signal generator (given to four significant figures). Errors and imprecision between f and actual forcing frequency, and slow frequency drifts, caused substantial "blurring" in the maps because we could not synchronize data samples with a specific forcing phase ϕ_0. Nonetheless, the experimental Poincaré maps are sufficiently clear to display the relevant fixed points and overall structures of the strange attractor.

All the experiments described below are done with magnet spacing $d=39.3$ mm and offset zero, corresponding to the restoring forces shown in Fig. 6.

5.1. Small forcing amplitudes: periodic orbits

For small forcing, the topology of the Poincaré map $\mathbf{P}$ is similar to the unforced case: i.e., the time $T=1/f$ flow map of Eq. (6) with $V_0=0$. The saddle and spiral sinks of Fig. 7(a) become saddle-type and sink-type period-1 orbits. Thus, $\mathbf{P}$ has two stable sinks and a saddle point with stable and unstable manifolds similar to those of Fig. 7(a); in particular, for fixed $\delta>0$ and sufficiently small P, the stable and unstable manifolds do not intersect, and the stable manifold still forms a 1-dimensional set that separates the domains of attraction of the sinks.

In our weakly damped case, in addition to low-amplitude periodic oscillations, a large-amplitude periodic motion encircling all three equilibria appears for modest values of P (cf. [4, p. 87]). Fig. 11(a) shows an example with the three stable period-1 orbits projected onto the (v_1, v_2)-plane, illustrating that higher harmonics exist. Estimates of points at which these orbits intersect the cross section Σ_0, shown in red, indicate substantial blurring due to lack of synchrony between forcing phase and Poincaré samples. Estimates for the fixed point of the large orbit are especially variable, due to its higher velocity. In spite of this, comparison with the orbits and fixed points of Fig. 11(b), predicted by numerical simulation of the full model, reveals good quantitative agreement, allowing for the fact that the (average) phase at which experimental Poincaré samples are taken differs by approximately π from the value $\phi_0=0$ used for simulated data.

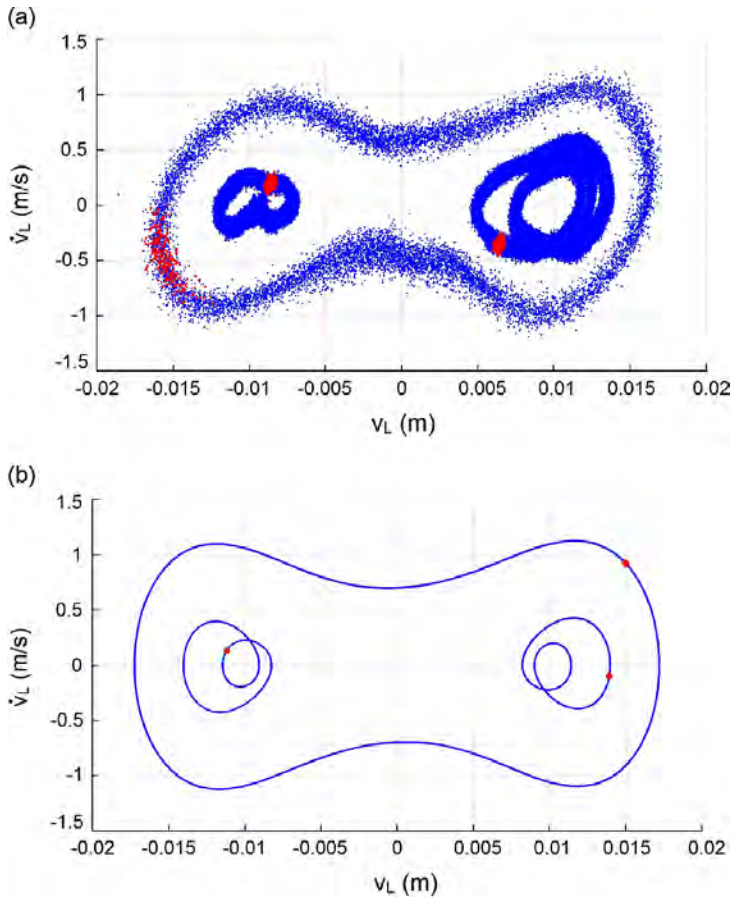

Fig. 11. (a) Projected orbits (blue) and corresponding fixed points of Poincaré map (red) from experimental data with $f=11.8$ Hz and $A_0=2.9$ mm ($P=25.0$). (b) Projected orbits and corresponding fixed points of Poincaré map from numerical simulations of full model with the same forcing parameters as (a). (For interpretation of the references to color in this figure caption, the reader is referred to the web version of this paper.)

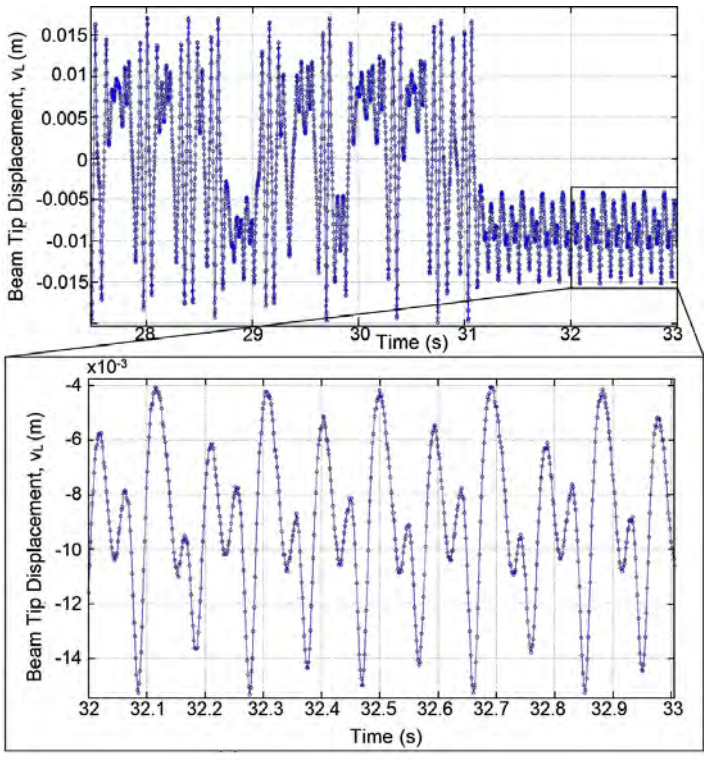

Fig. 12. Experimental time series for $f=10.43$ Hz and $A_0=3.95$ mm ($P=26.6$), showing transition from chaotic to period-2 (or possibly period-4) motion, with blown-up version of the latter. Slight changes in forcing frequency may prevent exact periodicity.

5.2. Large forcing amplitudes: transient and sustained chaos

As noted in Section 1, perturbation of the homoclinic orbit in the integrable case of Eq. (12) with $\delta = P = 0$ reveals that, as P increases for all other parameters fixed and $\delta > 0$ and small, the stable and unstable manifolds of the saddle point first touch at a critical value $P = \delta P_c(\alpha, \beta, \omega)$. Specifically, using Melnikov's method [23] and taking the cubic approximation, for which the necessary integrals can be evaluated explicitly, we find

$$P_c = \frac{4}{3}\left[\frac{\delta\alpha^{3/2}}{\pi\omega\sqrt{2\beta}}\right]\cosh\left(\frac{\pi\omega}{2\sqrt{\alpha}}\right). \tag{14}$$

See [7, Section 2.3] and [4, Section 4.5] for details, but note that in Eqs. (2.19) and (2.20) of [7] the hyperbolic functions cosech and sech should read sech and cosh respectively. For the experimentally derived cubic parameters, $\delta = 6.2$ and $f = 10.43$ Hz, the forcing frequency used for the following studies, $P_c \approx 4.89$, corresponding to $(A_0)_c \approx 0.73$ mm. (Recalling that $\alpha = \mathcal{O}(10^4)$ and $\beta = \mathcal{O}(10^8)$, δv_L and $P\cos(\omega t)$ are indeed small pertubations.) For $P > P_c$ we expect to see evidence of transient chaos in which orbits intermittently oscillate about the left and right equilibria before settling into periodic motions about one of them, or possibly encircling all three equilibria, as in Fig. 11. Moreover, for possibly higher values of P, we expect sustained chaotic motions characteristic of a strange attractor.

Fig. 12 shows an example of transient chaos that settles on a stable period-2 (or possibly period-4) orbit after some 31 s (the segment [27.5, 33] s is shown: small fluctuations in forcing frequency and noise in strain gauge signals perturb the orbit, making it difficult to distinguish period 2^n from 2^{n+1}). The corresponding Poincaré map appears in Fig. 13(a), with colder (blue) colors indicating points from the early transient and hotter (yellow, red) points from later samples. In contrast, the Poincaré map of Fig. 13(b), obtained for the same forcing frequency and 9 percent higher amplitude, indicates that a strange attractor occupies the same general region of phase space explored by the transient chaos of Figs. 12 and 13(a). Fig. 14 shows the segment [801,815] s of the time series from which Fig. 13(b) was derived, a part of which is blown up to reveal the mixture of oscillations about the two (now unstable) buckled states, separated by oscillations about all three equilibria of the unforced system.

While subharmonic periodic motions, such as those shown in Figs. 12 and 13(a), can occur, linear damping implies that the Poincaré map $\mathbf{P}$ uniformly contracts areas. In fact $\det(\mathbf{DP}) = \exp(-2\pi\delta/\omega) < 1$ for any single-degree-of-freedom,

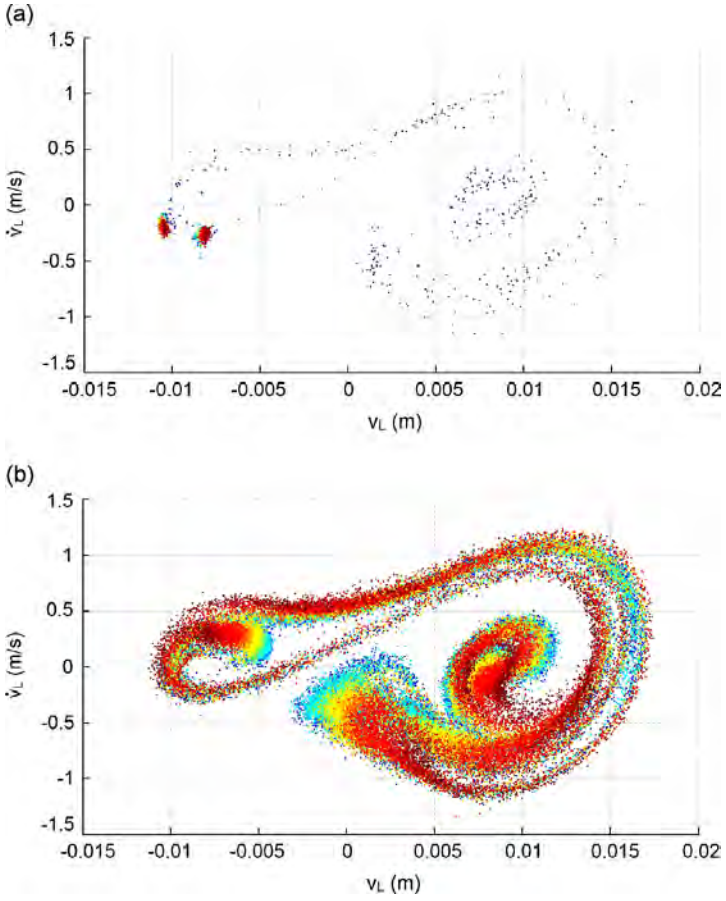

Fig. 13. Poincaré maps from experimental data for $f = 10.43$ Hz showing (a) transient chaos followed by attraction to a periodic orbit for $A_0 = 3.95$ mm ($P = 26.6$), and (b) chaotic motion sustained for over 2 h for $A_0 = 4.31$ mm ($P = 29.0$). Colder (resp. hotter) colors indicate points taken earlier (resp. later) in the time series. Color gradients in (b) indicate slow change in forcing frequency that affects the attractor's structure. (For interpretation of the references to color in this figure caption, the reader is referred to the web version of this paper.)

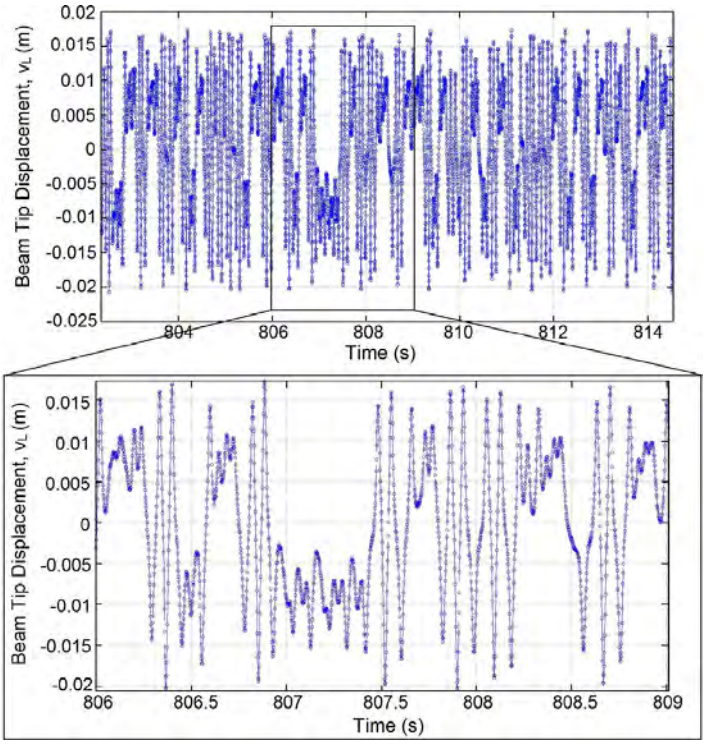

Fig. 14. Experimental time series for $f=10.43$ Hz and $A_0=4.31$ mm ($P=31.6$), showing sustained chaotic motion.

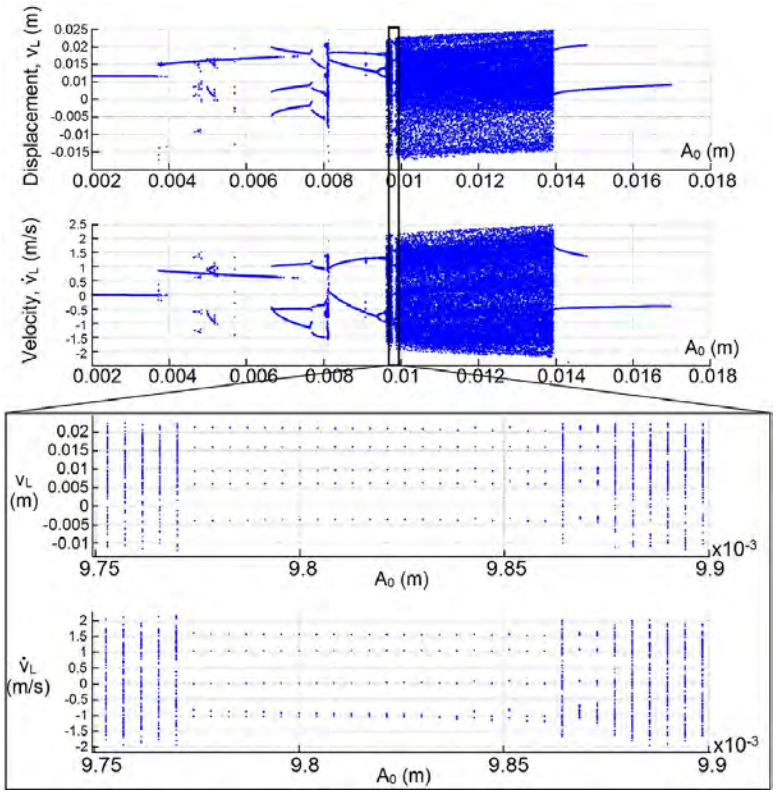

Fig. 15. Bifurcation diagram for 9.75 mm $\leq A_0 \leq$ 9.90 mm, showing a window of stability for a period-5 orbit between parameter ranges for which chaotic motions occur.

periodically forced oscillator with linear damping. This implies that **P** cannot possess an invariant closed curve, because the area of the interior of such a curve would be preserved under iterates of **P**. Hence the flow of Eq. (12) cannot contain an invariant torus, and so cannot exhibit quasiperiodic motions [4]. Nonetheless, complicated bifurcation sequences can occur as parameters vary. Fig. 15 shows a bifurcation diagram for $A_0 \in [2, 17]$ mm in which successive windows of stable periodic

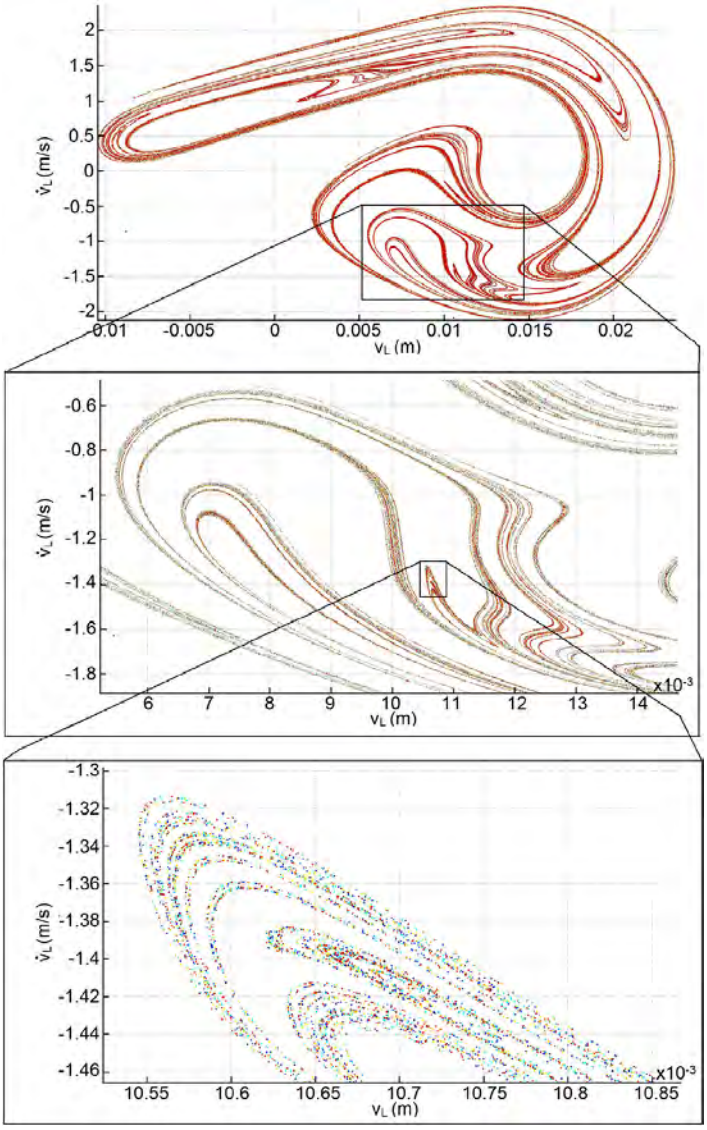

Fig. 16. Poincaré map for $f=10.43$ Hz and $A_0=12$ mm computed from numerical simulations of the full model, showing an apparent strange attractor with successive magnifications to illustrate its fractal structure. Colors indicate timing of samples, as in Fig. 13. (For interpretation of the references to color in this figure caption, the reader is referred to the web version of this paper.)

motions appear, with a blow-up of the range [9.75, 9.9] mm, illustrating a band of period five orbits between regions of chaos (cf. [7, Figs. 6 and 7], where a period-5 window was found for Düffing's equation).

Finally, Fig. 16 shows the Poincaré map computed from the full model for $f=10.43$ Hz and the higher amplitude $A_0=12$ mm, showing a similar, larger qualitative structure to the experimental map of Fig. 13(b). The simulation was run for over 2 h of real time, representing almost 5×10^6 iterates of the map. Precise sampling in the simulation and constant forcing frequency allows us to detect small features and illustrate the nested fractal structure typical of an attractor containing transverse homoclinic points that lies in the closure of an unstable manifold [4, Chapter 5]. Hot and cold colors remain mixed throughout the fractal structure, showing that it represents the long-term asymptotic behavior of the solution, in contrast to the experimental map of Fig. 13(b) in which a slow frequency drift has caused the attractor to shift from the blue and green regions to the red.

Computation of a power spectrum from this time series (not shown here) revealed a function of the form $K\,\mathrm{sech}^2(kf)\sim\exp(-kf)$, exponentially decaying for f large, as predicted in [24] and observed in [25]. This and related results, including further bifurcation diagrams showing period doubling and chaotic bands punctuated by windows of stable periodic orbits, can be found in [14].

6. Conclusions and discussion

This paper supplements an earlier theoretical and experimental study of a prototypical strange attractor [1]. Specifically, we carry out explicit calculations of the magnetic field experienced by a slender steel beam mounted in a frame that carries

two strong rare-earth magnets, inducing a multi-well potential energy function. We construct a relatively inexpensive experimental device[1] and show that a single mode projection of the governing partial differential equation, incorporating the spatially varying magnetic field, predicts buckled equilibria and natural frequencies within 10 percent (essentially, within experimental error). We compare a "full" model derived from the magnetic field calculations with two versions of the classical cubic Düffing equation, respectively having parameters fitted to that force field, and derived directly from the experimental rig. Then, focussing on the two-well case, we confirm that the experiment and model also predict chaotic transients, subharmonic periodic motions, and sustained non-periodic responses characteristic of strange attractors.

The magneto-elastic Duffing oscillator continues to play a valuable instructional role in nonlinear vibrations and dynamical systems theory more generally. In fact the experimental apparatus was built, and the analyses described here were carried out by the first author over some seven months, as a senior undergraduate thesis project. Almost all of the equipment needed, perhaps excepting the compact shaker, will be found in a typical engineering department laboratory, leading us to propose that similar devices can be fabricated for instructional purposes in teaching about electro-mechanical systems, both to exercise students' design and predictive abilities, and to excite, and partially satisfy, their curiosity about chaotic dynamics.

Acknowledgments

Jee Ian Tam thanks the Department of Mechanical and Aerospace Engineering for a John Marshall II Memorial Award and the Donald Jansson Dike Award, and thanks the School of Engineering and Applied Science for additional funds that enabled construction of the experimental apparatus, and generally supported his senior thesis research. We also thank the anonymous reviewers for pointing out minor errors and making suggestions that improved the paper.

References

[1] F.C. Moon, P.J. Holmes, A magnetoelastic strange attractor, *Journal of Sound and Vibration* 65 (2) (1979) 275–296. Also see Addendum, *Journal of Sound and Vibration* 69 (2) (1980) 339.
[2] G. Düffing, *Erzwungene Schwingungen bei Veränderlicher Eigenfrequenz*, F. Vieweg u. Sohn, Braunschweig, 1918.
[3] A.H. Nayfeh, D.T. Mook, *Nonlinear Oscillations*, Wiley, New York, 1979.
[4] J. Guckenheimer, P. Holmes, *Nonlinear Oscillations, Dynamical Systems and Bifurcations of Vector Fields*, Springer-Verlag, New York, 1983 (sixth printing, 2002).
[5] F.C. Moon, *Chaotic Vibrations*: *An Introduction for Applied Scientists and Engineers*, Wiley, New York, 1987.
[6] F.C. Moon, *Chaotic and Fractal Dynamics*: *An Introduction for Applied Scientists and Engineers*, Wiley, New York, 1992.
[7] P. Holmes, A nonlinear oscillator with a strange attractor, *Philosophical Transactions of the Royal Society A* 292 (1979) 419–448.
[8] P. Holmes, J.E. Marsden, A partial differential equation with infinitely-many periodic orbits: *chaotic oscillations of a forced beam*, *Archive for Rational Mechanics and Analysis* 76 (1981) 135–166.
[9] P. Holmes, J.E. Marsden, Horseshoes in perturbations of Hamiltonian systems with two degrees of freedom, *Communications in Mathematical Physics* (1982) 523–544, 20.
[10] J. Awrejcewicz, D. Sendkowski, How to predict stick-slip chaos in $\mathbb{R}^4$, *Physics Letters A* 330 (2004) 371–376.
[11] V.A. Krysko, J. Awrejcewicz, I.E. Kutepov, N.A. Zagniboroda, I.V. Papkova, A.V. Serebryakov, A.V. Krysko, Chaotic dynamics of flexible beams with piezoelectric and temperature phenomena, *Physics Letters A* 377 (2013) 2058–2061.
[12] T. Kanamaru, Duffing oscillator, *Scholarpedia* 3 (2008) 6737. ⟨http://www.scholarpedia.org/article/Duffing_oscillator⟩.
[13] N. Derby, S. Olbert, Cylindrical magnets and ideal solenoids, *American Journal of Physics* 78 (3) (2010) 229–235.
[14] J.I. Tam, Numerical and Experimental Investigations into the Nonlinear Dynamics of a Magneto-Elastic System, Senior Thesis, Department of Mechanical and Aerospace Engineering, Princeton University, 2013.
[15] K.D. Hjelmstad, *Fundamentals of Structural Mechanics*, Springer Science, New York, 2010.
[16] W.T. Thompson, M. Dahleh, *Theory of Vibration with Applications*, 5th edition, Prentice-Hall, Upper Saddle River, NJ, 1993.
[17] F.C. Moon, Y.H. Pao, Magnetoelastic buckling of a thin plate, *Transactions of the ASME Journal of Applied Mechanics* 35 (1968) 53–58.
[18] F.C. Moon, Y.H. Pao, Vibration and dynamic instability of a beam-plate in a transverse magnetic field, *Transactions of the ASME Journal of Applied Mechanics* 36 (1969) 92–100.
[19] C. Moosbrugger, F. Cverna, *Electrical and Magnetic Properties of Metals Data Book* (06333G), ASM International, Materials Park, OH 44073, 2000.
[20] M.T. Heath, *Scientific Computing*: *An Introductory Survey*, McGraw-Hill, New York, 2001.
[21] N.J. Kasdin, *Engineering Dynamics*: *A Comprehensive Introduction*, Princeton University Press, Princeton, NJ, 2011.
[22] T. Poston, I. Stewart, *Catastrophe Theory and its Applications*, Pitman, London, UK, 1976.
[23] V.K. Melnikov, Stability of the center to time periodic perturbations, *Transactions of the Moscow Mathematical Society* 12 (1963) 1–56.
[24] V. Brunsden, P. Holmes, Power spectra of strange attractors near homoclinic orbits, *Physical Review Letters* 58 (17) (1987) 1699–1702.
[25] V. Brunsden, J. Cortell, P. Holmes, Power spectra of chaotic oscillations of a buckled beam, *Journal of Sound and Vibration* 130 (1989) 1–25.

[1] The cost of the entire setup, excluding signal generator, was approximately $4200, the major expense (almost $3900) being the shaker.